

Effect of laser beam offset on dissimilar laser welding of tantalum to 304 stainless steel

Xiangyi Meng (✉ mxy7199@163.com)

Harbin Industry University: Harbin Institute of Technology

Fan Song

Hongbo Xia

<https://orcid.org/0000-0003-0405-2345>

Xi Chen

Xiaoye Zhao

Bo Chen

Xiaoguo Song

Caiwang Tan

Research Article

Keywords: Laser welding, Tantalum, 304 stainless steel, interfacial microstructure, mechanical properties

Posted Date: June 7th, 2022

DOI: <https://doi.org/10.21203/rs.3.rs-1643879/v1>

License: © ⓘ This work is licensed under a Creative Commons Attribution 4.0 International License.

[Read Full License](#)

Effect of laser beam offset on dissimilar laser welding of tantalum to 304 stainless steel

Xiangyi Meng ^a, Fan Song ^b, Hongbo Xia^{c*}, Xi Chen ^a,

Xiaoye Zhao ^a, Bo Chen ^a, Xiaoguo Song ^a, Caiwang Tan ^a

^a State Key Laboratory of Advanced Welding and Joining, Harbin Institute of Technology, Harbin 150001, China

^b Shanghai Institute of Space Propulsion, Shanghai 201114, China

^c School of Mechanical Engineering, Yangzhou University, Yangzhou 225127, China

* Corresponding author: **Hongbo Xia (jssrxhb@126.com)**

Abstract: Cylinders made of tantalum (Ta) and tubes made of 304 stainless steel (304SS) were successfully joined by laser welding under different offsets. The experimental results indicated that satisfactory weld formations were obtained. The fusion zone (FZ) was found to consist of the Fe-Cr solution and the Fe₂Ta phase. In addition, the intermetallic compounds (IMCs) layer was generated at Ta/FZ interface. When the laser beam offset was -0.2 mm (0.2 mm laser beam offset on the 304 stainless steel side), the interfacial IMC consisted of Fe₂Ta. Thicker IMC with the compositions of Fe₂Ta+FeTa was generated at offsets of 0 mm (center) and +0.2 mm (0.2 mm laser beam offset on the Ta side). Numerical simulation results showed that the interfacial peak temperature would be increased when the laser beam offset from 304 stainless steel side to Ta side, which led to the thicker IMC and new generation of FeTa. The microhardness in the FZ also fluctuated since the FZ was composed of hard Fe₂Ta and soft Fe-Cr solution. Tensile test results indicated that the highest value of 308.3 MPa was obtained under the laser beam offset of -0.2 mm.

Keywords: Laser welding, Tantalum, 304 stainless steel, interfacial microstructure, mechanical

properties

1. Introduction

Refractory metal tantalum (Ta) has excellent wear resistance and stable mechanical properties at high temperature [1, 2] and it is usually adopted as heaters of cathode assembly in aerospace electric propulsion systems. 304 stainless steel (304SS) exhibits high strength and strong corrosion resistance and it is usually employed as supporting tubes for the heater cylinder. Therefore, obtaining a satisfactory connection between tantalum cylinder and 304 stainless steel tube is essential, and welding can provide a solution. Obtaining a refractory metal/steel dissimilar joint with high strength faces great challenges due to the huge differences in thermal physical properties and metallurgical performance between base metals [3-5]. Laser welding technology can provide a solution since it has the advantages of small heating area, large welding speed, fast heating and cooling rate, and high automation [6-8]. Therefore, obtaining a satisfactory laser welded Ta/304SS joint is significant for aerospace.

For the refractory metal/steel joint, weld formation and microstructure determined the joint strength as the dominant factors. For instance, Zhang et al. [9] found that the coarse surface of Mo/stainless steel joint would cause the generation of cracks which would finally reduce the joint strength. Ali et al. [10] discovered that pits and extrusion in the Nb/steel joint would evolve as the origination of cracks, leading to the reduction of joint strength (The joint with and without pits and extrusion exhibited the tensile strength of 82 MPa and 170 MPa, respectively). Yu et al. [11] noticed that a thinner intermetallic compounds (IMCs) layer was more beneficial for the improvement of TZM/stainless steel dissimilar joints. The joint strength increased from 165 MPa to 313 MPa when interfacial IMCs thickness reduced from 10 μm to 0 μm .

From above researches, it could be found that a satisfactory weld formation and an interfacial IMC with thinner thickness were beneficial for the joint strength, which had a great association with welding heat input. For instance, Gao et al. [12] found that excessive heat input would cause the severe fluctuation of molten pool and finally lead to the formation of coarse weld appearance. Sang et al. [13] indicated that excessive heat input in the Ta/GH3218 joints would cause the generation of porosities (due to the excessive melting of base metals under excessive high temperature) and cracks (due to the huge asynchrony of melting and cooling under excessive peak temperature). Chen et al. [14] reported that thick IMC generated in the Ta/304SS joint due to the severe diffusion of atoms resulting from melted base metals at excessive heat input. In the above researches, the coarse weld appearance, porosities and thick IMC which resulted from unreasonable heat input had a negative effect on the joint strength. During laser welding, the heat input could be flexibly adjusted by the variations of laser beam offset [12]. By adopting laser beam offset, the heat input could be distributed in a more reasonable method and inhibit the aforementioned defects [9]. Nevertheless, researches about the laser welding of Ta cylinder to 304 stainless steel tube (to form heterogeneous structure) under various laser beam offsets were rarely reported.

Therefore, the aim of this study was to investigate the influence of laser beam offsets on the welding formation and microstructure of the laser welded Ta cylinder/304SS tube joints. Then the interfacial thermal cycles were calculated to reveal the interfacial heat distribution under various laser beam offsets and further provide analysis for the welding formation and interfacial microstructure evolutions. Finally, tensile tests were conducted to clarify the joint strength variations under different laser beam offsets.

2. Experimental procedures

2.1 Base metals

Rolling-stated tantalum and austenite 304 stainless steel were employed as base metals in this work as seen in Fig. 1. Chemical compositions of Ta and 304 stainless steel were presented in Table 1. The detailed longitudinal sections of cylindrical 304SS and tubular Ta and the sectional views of them were exhibited in Fig. 2. The A face (as marked in Fig. 2) of the 304SS workpiece was fitted to the B face (as marked in Fig. 1) of Ta workpiece during the assembly process. Both of the A and B face had an outer diameter of 8 mm and an inner diameter of 6 mm. Therefore, 304SS cylinder and Ta tube was assembled together as a lock butt joint.

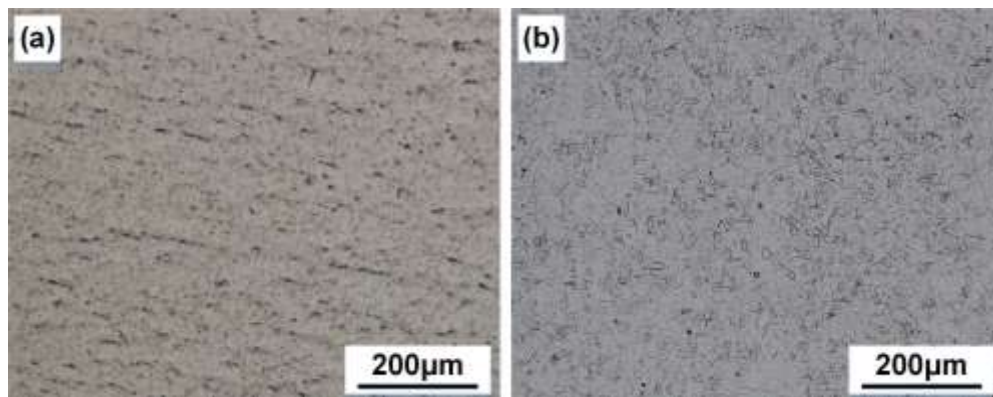


Fig. 1 Optical images of base metals: a Ta, b 304SS.

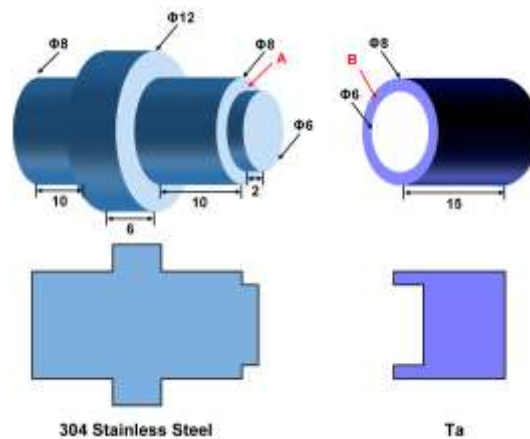


Fig. 2 Detailed geometric dimensions and sectional views of 304SS (left) and Ta (right) (units: mm).

Table 1 Chemical composition of the base metals (wt.%).

Element	Ta	C	Cr	Ni	Ti	Fe
Ta	≥99.99	0	0	0	0	0
304 SS	0	≤0.12	17-19	8-11	0.5-0.8	Bal.

2.2 Laser welding process

Fig. 3 showed the schematic diagram of laser welding Ta to 304SS. The welding process was carried out by an IPG YLS-6000 fiber laser system with 6-kW maximum output power, 1070-nm laser beam wavelength, 8-mm mrad beam parameter product, and 0.6-mm-diameter focused beam. The energy distribution for the focused laser beam was Gaussian volume. Ta and 304SS were assembled by a special rotary fixture. KR16-2 KUKA robot with a six-axis was employed in the process. Argon gas was used as shielding gas to prevent oxidation of molten metals. Table 2 listed the laser welding processing parameters adopted in this study. Laser beam offset indicated the distance between laser spot center and the Ta/304SS interface. When the center of the laser spot was irradiated on the 304SS, the offset was recorded as a negative value, while on the Ta, the offset was recorded as a positive number. The laser beam offset ranged from -0.6 mm (0.6 mm laser beam offset on 304SS side) to +0.2 mm (0.2 mm laser beam offset on Ta side). Define the joints obtained under the laser beam offsets of -0.2 mm, 0 mm, and +0.2 mm as joint 1, joint 2, and joint 3, respectively. Before the welding process, standard chemical cleaning and mechanical polishing were adopted to remove the oxidation films and contaminations of base metals.

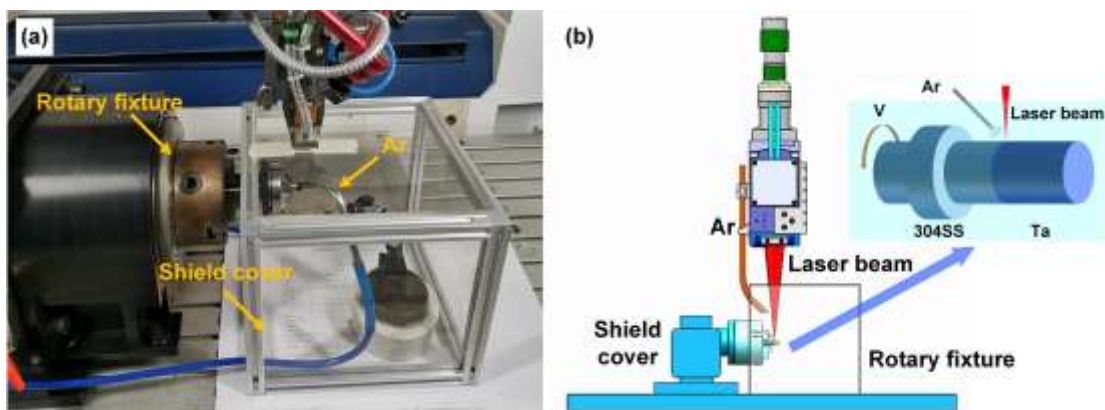


Fig. 3 Schematic diagram of laser welding of Ta to 304SS.

Table 2 Detailed process parameters employed in this work.

Adopted parameters	Values
--------------------	--------

Laser power, W	1200
Welding speed, mm/s	7.4
Defocused distance, mm	0
Flow rate of shielding gas, L/min	15

2.3 Numerical simulation

The commercial finite element method (FEM) software ABAQUS was adopted to calculate the thermal cycles during laser welding. The schematic diagram of the numerical models and divided meshes were demonstrated in Fig. 4. The model of 304SS was simplified to a cylinder with a tab by removing the part away from the weld, and the specific dimensions were shown in the label in Fig. 4. Finer meshes (0.1 mm) and coarse meshes (0.5 to 1.0 mm) were respectively generated at the welding zone and outer regions to reduce computational duration based on acceptable accuracy. All the meshes were set as eight nodes and hexahedron elements. The total number of elements for Ta and 304SS were 6852 and 8748, respectively.

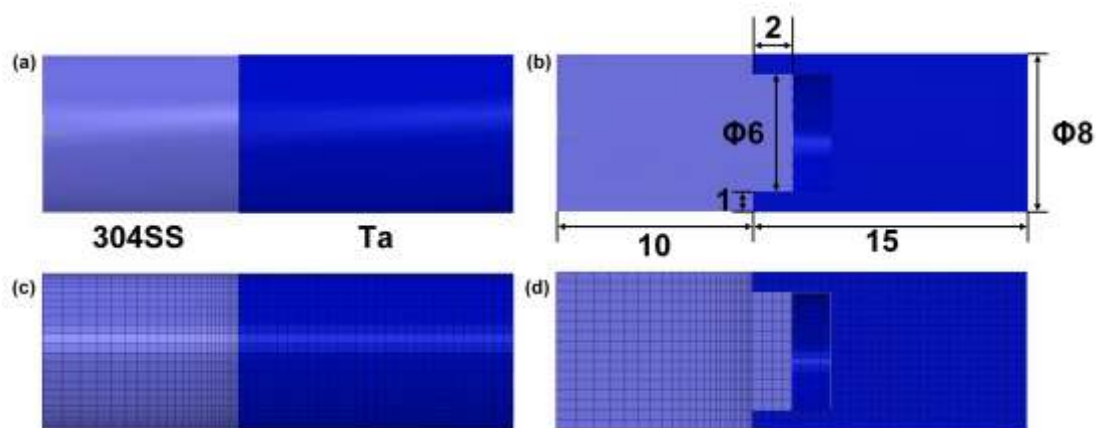


Fig. 4 Developed numerical models in this work: **a** developed geometric model for 304SS and Ta; **b** geometric dimensions for 304SS and Ta (unit: mm); **c** generated meshes for the model; **d** generated meshes at the cross section for the model.

Considering the deep penetration characteristics of laser welding in this study, combined Gauss surface+volume heat source was adopted as seen in Eqs. (1-3) [15]:

$$Q_s(x, y, z) = \frac{3\varphi\eta P}{\pi r_s^2} \exp\left(-3 \frac{(x - x_{laser})^2 + (y - y_{laser})^2}{r_s^2}\right) \quad (1)$$

$$Q_v(x, y, z) = \frac{6(1-\varphi)\eta P}{\pi r_v H (Hm + 2r_v)} \exp\left(-3 \frac{(x - x_{laser})^2 + (y - y_{laser})^2}{r_v^2}\right) \frac{r_v + mz}{r_v} \quad (2)$$

$$Q(x, y, z) = Q_s(x, y, z) + Q_v(x, y, z) \quad (3)$$

where Q_s is heat flux of Gauss surface heat source, Q_v is heat flux of Gauss volume heat source, Q is the total heat flux, φ is the ratio of surface heat source, η is the absorption coefficient of the laser beam, P is the total laser power, r_s and r_v are the radii of surface and volume heat source, respectively, H is the effective depth of volume heat source, m is energy distribution coefficient of volume heat source in the depth direction, x_{laser} , y_{laser} are the coordinates of laser heating center, and x , y , and z are the coordinates of laser heating center along x , y , and z directions, respectively. The material properties in the models were quoted from data provided in the literature [16, 17] and presented in Fig. 4. The densities of Ta and 304SS were set as constant values of 1660 kg/m^3 and 7930 kg/m^3 , respectively.

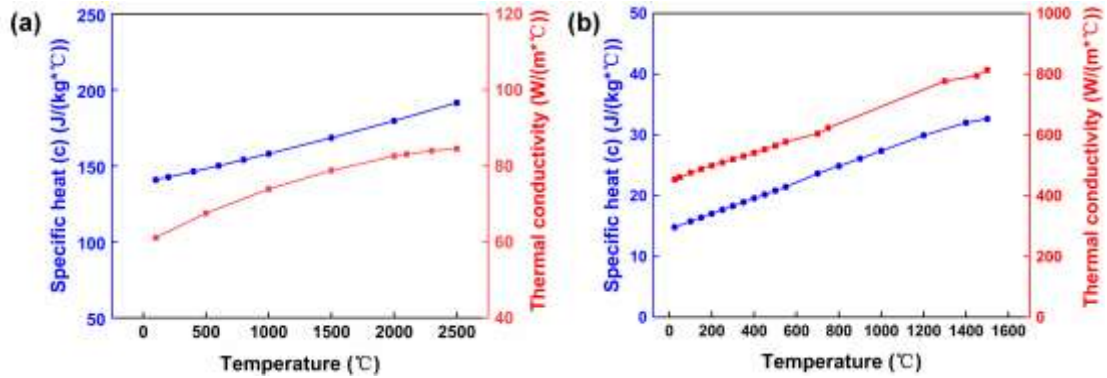


Fig. 5 Temperature dependent thermo-physical properties for base metals: **a** Ta [16]; **b** 304SS [17].

Natural boundary condition on the workpiece was expressed as follows:

$$k \frac{\partial t}{\partial x} - Q_s + h(T - T_0) + \sigma \varepsilon (T^4 - T_0^4) = 0 \quad (4)$$

where k is the thermal conductivity, Q_s is the heat flux, h is the convection heat transfer coefficient, σ is Stefan-Boltzmann Constant ($5.67 \text{ W}/(\text{cm}^2 \cdot \text{K}^4)$), ε is the emissivity of the metal surface, and T_0

is the environment temperature (20°C).

In order to simplify the boundary conditions, a total heat transfer coefficient was introduced to sum convection and radiation coefficients in the model [18] as presented in Eq. (5)

$$h_{eff} = 2.4 \times 10^{-3} \times \varepsilon \times T^{1.61} \quad (5)$$

2.4 Analysis methods

Optical microscopy (OM) and field emission scanning electron microscopy (SEM) were employed to observe the cross-sectional and typical fracture surface morphology. The elements distribution near the interface were analyzed by Energy Dispersive Spectrometer (EDS), and the interfacial phase compositions at the fractured surface were confirmed by X-ray diffraction (XRD). The joint strengths obtained under various laser beam offsets were evaluated by lap shear tests with a universal testing machine of 1 mm/min at room temperature. Then the joint strength of the workpiece was calculated as following equations:

$$\sigma = \frac{F}{\pi(R^2 - r^2)} \quad (6)$$

where the σ is the joint strength, F is the fractured force, R is the outer diameter of the tantalum cylinder and r is the inner diameter of it. The average tensile strength of three specimens was calculated to improve the accuracy.

3. Results and discussion

3.1 Welding formation

Figs. 6(a-c) showed the weld appearances of the tantalum/304 stainless steel joints with different laser beam offsets while Figs. 6(d-f) presented corresponding cross sections of the joints. Two typical welding and brazing interfaces were produced in these joints. Satisfactory weld formations without cracks or undercut were obtained under these welding conditions, which

indicated that the welding parameters used in this work were reasonable.

The cross-sectional morphology of joint 1 was shown in Fig. 6d. A typical welding-brazing joint was observed to form, namely that the steel was melted to produce a fusion zone (FZ) while the Ta was almost solid. Then the melted steel spread along the solid Ta to produce a brazing interface both as seen in regions A and B. The cross-sectional morphology of joint 2 was shown in Fig. 6e. Ta base metal was slightly melted at the top surface due to the smaller distance between the laser heating center and the top surface of Ta base metal. Welding-brazing interface was found in regions A and B. In addition, the fusion depth was also decreased and an obvious reaction layer could be observed at the region C. The cross-sectional morphology of joint 3 was shown in Fig. 6f. Welding-brazing interface was also observed in this joint and the weld width of Ta base metal at the top surface became larger. This was caused by the laser beam offset on Ta base metal. Furthermore, the joint had the shallowest fusion depth compared with the previous two joints.

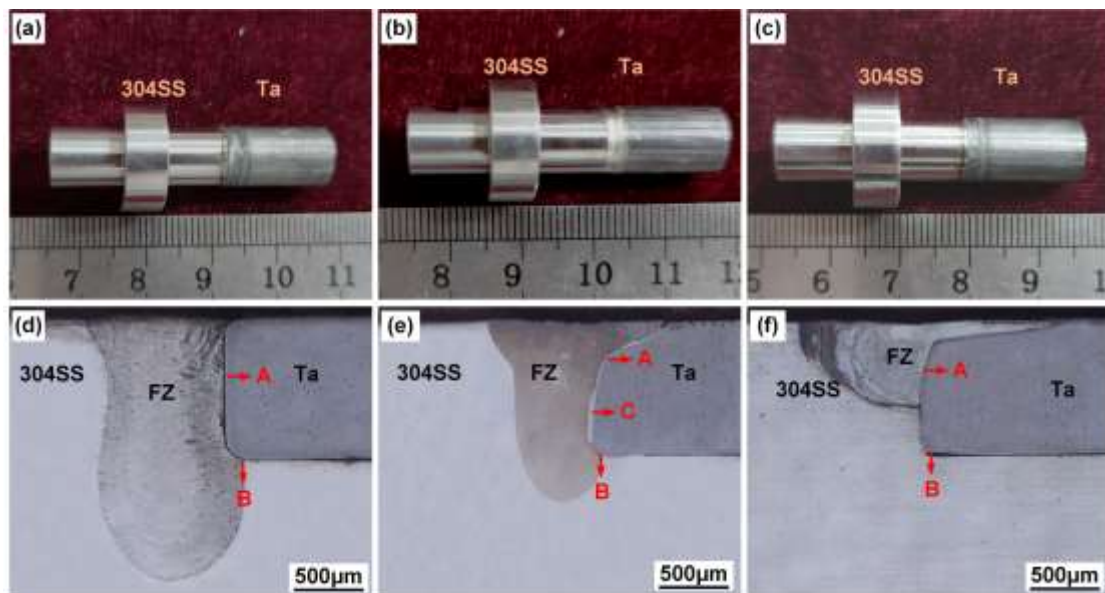


Fig. 6 Appearances and cross sections of Ta/304SS joints produced with various laser beam offsets: (a, d) -0.2 mm; (b, e) 0 mm; (c, f) +0.2 mm.

3.2 Microstructure

Fig. 7 presented the microstructure and element distribution for joint 1 and Table 3 presented

the measured chemical compositions in the selected regions. The joint was mainly connected by the brazing interface as shown in Fig. 7a. Fig. 7b demonstrated the microstructure of the fusion zone. It consisted of gray matrixes and scattered phases. The gray matrixes and scattered phases were determined as Fe-Cr solutions since they mainly contained 75.95 at.% Fe and 22.13 at.% Cr, which was also observed in previous studies [14]. The content of Ta was as low as 1.93 at.% and this implied that only limited Ta element was diffused to the fusion zone due to its solid state during the welding process. Fig. 7c showed the brazing interface at the upper region of Ta base metal, which was remarked as region c in Fig. 7a. An obvious Fe-Ta-Cr elemental transition layer was produced at this region and this indicated that an interfacial IMC formed. The formation of interfacial IMC could be also proved by the stable Fe-Ta elemental diffusion zone as seen in Fig. 7d. According to the EDS results, this IMC layer was also Fe_2Ta since it had the compositions of 81.12 at.% (Fe + Cr) and 18.88 at.% Ta [14]. The interfacial IMC thickness became smaller from the top to the bottom at this region. This was caused by the reduction of peak temperature along the thickness direction, which was resulted from the larger distance to the laser heating area. Fig. 7e depicted the microstructure of region e in Fig. 7a. A transition layer was also produced between Ta and the FZ. According to the EDS tested results in Table 3, it contained 84.95 at.% (Fe+Cr) and 14.05 at.% Ta, which was proved to be Fe_2Ta . Fig. 7f presented the edge of the Ta/FZ interface at the bottom area as marked region f in Fig. 7a. An unbonded interface was observed to produce at this region due to the insufficient heat input, which was disadvantageous for the joint strength.

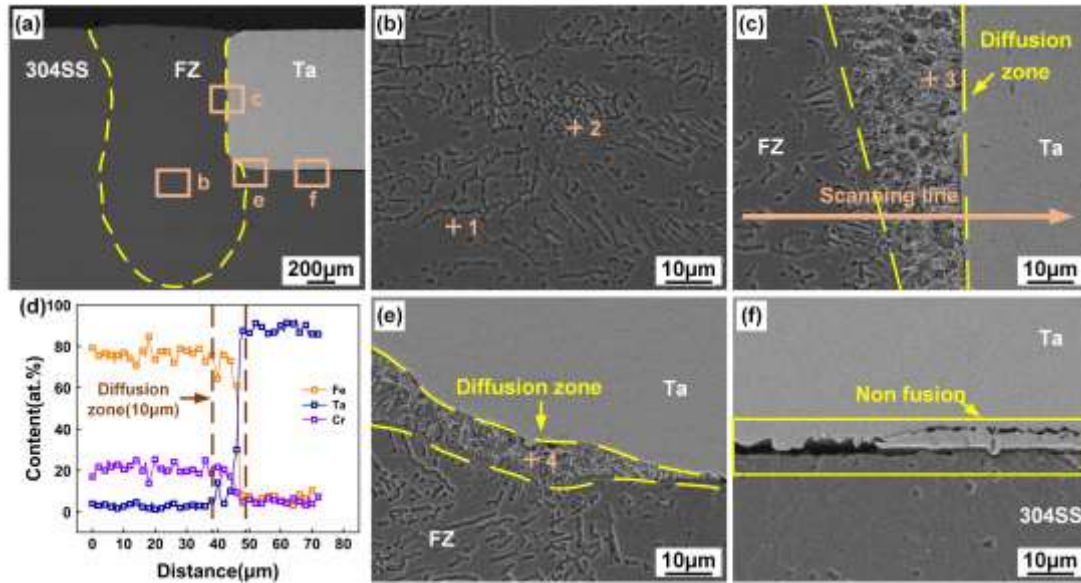


Fig. 7 Microstructural morphologies and EDS results for joint 1: **a** cross section; **b** FZ; **c** middle region; **d** line scanning results; **e** bottom of Ta; **f** unreacted region.

Table 3 Component of different points in Fig. 7 (at.%).

Position	Fe	Ta	Cr	Possible phases
1	75.94	1.93	22.13	Fe-Cr solution
2	76.94	2.44	20.62	Fe-Cr solution
3	63.81	18.88	17.31	Fe ₂ Ta
4	64.29	14.05	21.66	Fe ₂ Ta

Fig. 8 presented the microstructure and element distribution for joint 2 and Table 4 listed the measured chemical compositions in the selected regions. The top edge of Ta base metal was not square and this indicated that the Ta was partially melted. The observed results in the fusion zone, as marked in region b, were seen in Fig. 8b. In this region, the FZ consisted of gray matrixes and columnar crystals. The gray matrixes were determined as Fe-Cr solutions while the columnar crystals were determined as Fe₂Ta, which was different from joint 1. The generation of Fe₂Ta in the fusion zone was resulted from the slightly melting of Ta base materials as seen in Fig. 8a. The interface between melted Ta and FZ was remarked as region c and its corresponding microstructure was shown in Fig. 8c. Two different transition layers were found in this region: layer 1 nearby the FZ and layer 2 adjacent to the Ta substrate. According to the listed EDS results in Table 5, layer 1

was determined as Fe_2Ta (72.42 at.% (Fe + Cr) and 27.58 at.% Ta) while layer 2 was determined as FeTa (53.81 at.% (Fe + Cr) and 46.19 at.% Ta). Fig. 8d showed the Ta/FZ interface at the lower part of Ta base material. This interface was composed of extrusion in the vicinity of FZ as remarked by layer 3 and continuous diffusion zone as remarked by layer 4. The layer 3 was Fe_2Ta (72.42 at.% (Fe+Cr) and 27.58 at.% Ta) while the inner layer 4 was FeTa (48.68 at.% (Fe + Cr) and 51.32 at.% Ta). The elemental scanning results of this interface as seen in Fig. 8e also showed a stable atomic transaction zone occurred at this region, which indicated the formation of interfacial IMC. The microstructure at the bottom region of Ta was presented in Fig. 8f. Brazing occurred at the interface and a dendritic structure formed in the fusion zone. The dendritic structure was determined as Fe_2Ta , according to the EDS results listed in Table 4.

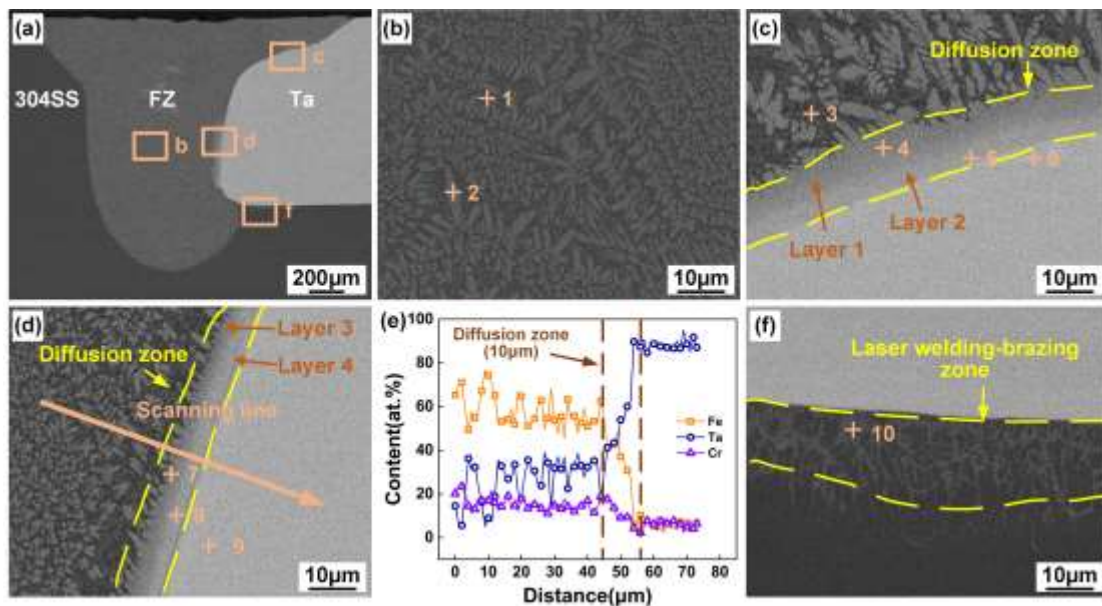


Fig. 8 Microstructural morphologies and EDS results for joint 2: **a** cross section; **b** FZ; **c** direct irradiation; **d** middle region; **e** line scanning results; **f** bottom of Ta.

Table 4 Component of different points in Fig. 8 (at.%).

Position	Fe	Ta	Cr	Possible phases
1	70.68	9.56	19.76	Fe-Cr solution
2	58.32	24.56	17.12	Fe_2Ta
3	70.78	9.73	19.49	Fe-Cr solution

4	58.34	27.58	14.08	Fe ₂ Ta
5	41.86	46.19	11.95	FeTa
6	4.27	93.16	2.57	Ta
7	58.34	27.58	14.08	Fe ₂ Ta
8	40.75	51.32	7.93	FeTa
9	3.80	93.43	2.77	Ta
10	61.98	14.68	23.34	Fe ₂ Ta

Fig. 9 presented the microstructure and element distribution for joint 3 and Table 6 listed the measured chemical compositions in the selected regions. The observed results in the FZ as marked in region b were seen in Fig. 9b. In this region, the FZ mainly consisted of a large number of dendritic and island-like Fe₂Ta phases which contained 75.48 at.% (Fe + Cr) and 24.52 at.% Ta as listed in Table 5. The generation of large amounts of Fe₂Ta in the FZ was attributed to the massive melting of Ta base materials. Fig. 9c showed the edge of the Ta/FZ interface at the top region as region c marked in Fig. 9a. Two different transition layers were also generated in this region, i.e. layer 1 nearby the FZ and layer 2 adjacent to the Ta base materials. According to the listed EDS results in Table 5, layer 1 was determined as Fe₂Ta since it had a composition of 73.65 at.% (Fe + Cr) and 26.35 at.% Ta. Layer 2 was detected as FeTa since it had a composition of 43.95 at.% (Fe + Cr) and 56.05 at.% Ta. The Ta/FZ interface at the lower part of FZ as region d was presented in Fig. 9d. This interface consisted of extrusion near the weld and continuous diffusion zone. These two zones were respectively marked as layer 3 and layer 4 as shown in Fig. 9d. According to the EDS results, layer 3 was identified as Fe₂Ta (71.04 at.% (Fe + Cr) and 28.96 at.% Ta) while the inner layer 4 was determined as FeTa (39.63 at.% (Fe + Cr) and 60.37 at.% Ta). The thickness of interfacial IMC in joint 3 was thicker than that in joint 1 and joint 2. This was caused by the closer proximity to the area of the laser heating center and the increase of interfacial heat input. Fig. 9e

showed the elemental scanning results of the interface as marked in Fig. 9d. The observed results indicated a stable atomic transition zone occurred at this region, which proved the formation of interfacial IMC. The morphology at the bottom region Ta was presented in Fig. 9f. An unfused area was produced in this region due to insufficient heat input.

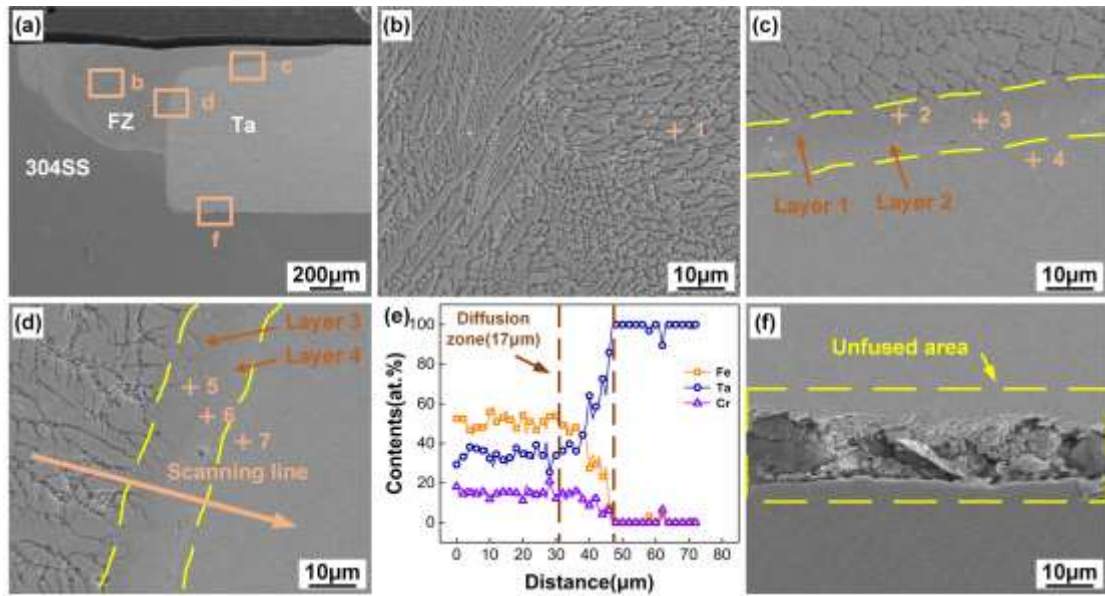


Fig. 9 Microstructural morphologies and EDS results for joint 3: **a** cross section; **b** FZ; **c** direct irradiation region; **d** middle region; **e** line scanning results; **f** unreacted region.

Table 5 Component of different points in Fig. 9 (at.%).

Position	Fe	Ta	Cr	Possible phases
1	60.24	24.52	15.24	Fe ₂ Ta
2	59.05	26.35	14.60	Fe ₂ Ta
3	39.97	56.05	3.98	FeTa
4	3.44	92.99	3.57	Ta
5	55.92	28.96	15.12	Fe ₂ Ta
6	35.64	60.37	3.99	FeTa
7	4.21	92.79	3.00	Ta

To better verify the influence of laser beam offset on the microstructure variations, the elemental distribution at three joints was observed and corresponding results were shown in Fig. 10. The EDS mapping results showed that the elemental distribution of Cr and Fe was identical, which

was due to the infinite solution between Cr and Fe elements. Less Fe and Cr but more Ta element was distributed in the FZ, as the laser beam offset on Ta side. Hence, it had a higher content of Fe-Ta IMC as seen in Figs. (7-9). In Fig. 10f, a Ta-rich area was produced and this caused the formation of Fe-Ta interfacial IMC as seen in Fig. 8d.

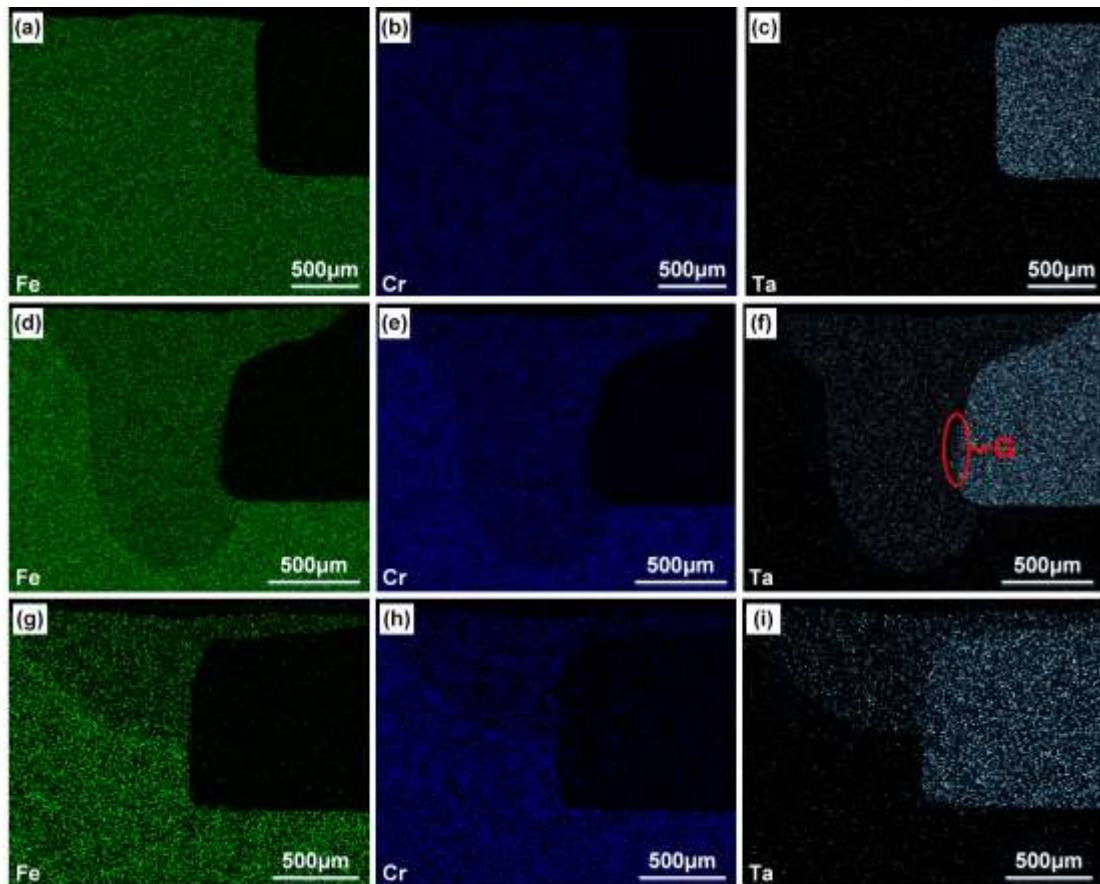


Fig. 10 EDS mapping results of Ta/304SS joints with different laser beam offsets: (a-c) -0.2 mm; (d-f) 0 mm; (g-i) +0.2 mm.

To further determine the interfacial microstructure evolutions under different laser beam offsets, micro-XRD tests were conducted in the region including the FZ and interface. Figs. 11a - 11c showed the test zone for these three joints, respectively, while corresponding results were presented in Fig. 11d. For joints 2 and 3, diffraction peaks of Fe_2Ta were discovered. It provided further evidence for the formation of Fe_2Ta in the two joints. The diffraction peak of Fe_2Ta was not indexed in joint 1, which had a good coincidence with SEM and EDS results as seen in Fig. 7 and Table 3,

respectively. It should be noticed that FeTa was not detected since the FeTa was only generated near the interface between the FZ and Ta in a small amount.

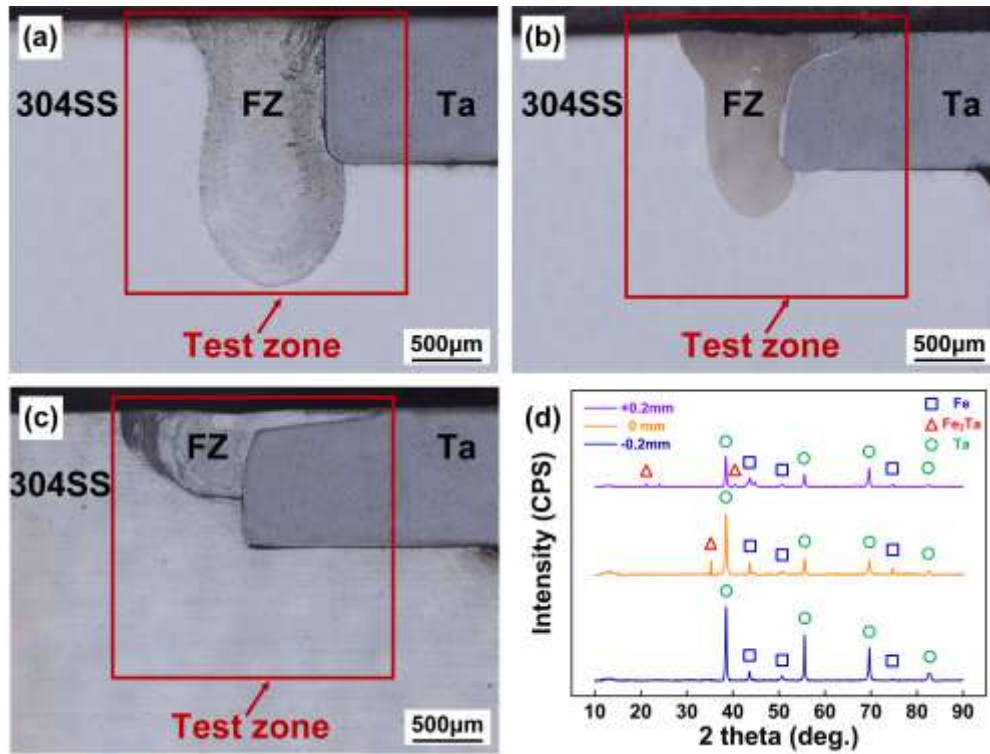


Fig. 11 Schematic diagram of the micro-XRD test zone for different Ta/304SS joints: **a** joint 1; **b** joint 2; **c** joint 3; **d** the results for the micro-XRD test.

3.3 Thermal cycles

The interfacial microstructure evolutions were closely associated with thermal cycles. Therefore, interfacial thermal cycles in this study were calculated. First, the reasonability of developed numerical models was verified by the comparisons between numerical and experimental weld profiles. Corresponding results were presented in Fig. 12 and detailed weld profile dimensions were listed in Table 6. The weld profile had a satisfactory coincidence between numerical and experimental results, which proved that the developed numerical model in this research was reasonable and trustworthy.

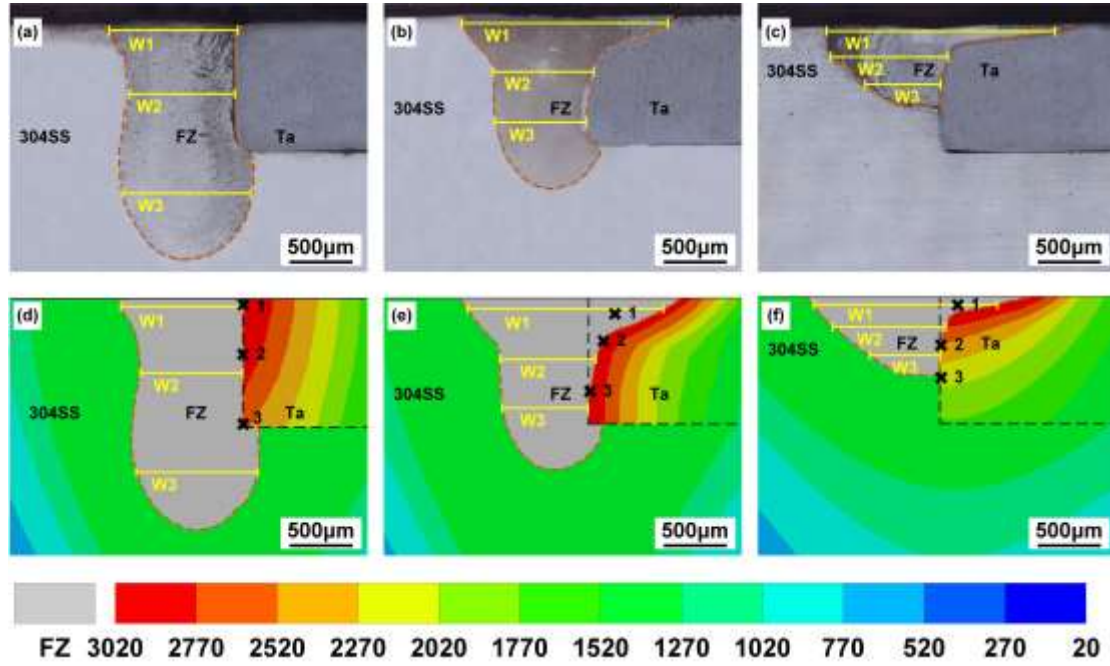


Fig. 12 Model verification for different joints obtained with different laser beam offsets: (a, d) -0.2 mm; (b, e) 0 mm; (c, f) +0.2 mm.

Table 6 The comparison of the width between simulated resulted and experimental joints.

Laser beam offset (mm)		W1 (μm)	W2 (μm)	W3 (μm)	Average relative error (%)
-0.2	Experimental	1017.6	832.0	1018.5	5.78%
	Numerical	929.32	806.5	961.6	
0	Experimental	1632.0	795.2	723.2	5.27%
	Numerical	1552.0	756.0	680.0	
+0.2	Experimental	1808.0	926.5	600.0	9.92%
	Numerical	1556.0	892.8	560.0	

Three points were selected from top to bottom along with the interface of these models as marked in Figs. 12(d-f). Their temperature histories were extracted and plotted as curves in Fig. 13, and the 3020°C marked in this figure indicated the melting point of Ta [16]. The 1775°C marked in Fig. 13 represented the generating temperature of Fe_2Ta , while the generating temperature of FeTa was above 1800°C [16]. The temperature history curves for joint 1 were shown in Fig. 13a. Only the peak temperature of point 1 reached the melting point of Ta (3020°C). It was consistent with the fact that only a small amount of Ta melted at the top as shown in Fig. 7. Fig. 13b presented the

temperature history curves corresponding to joint 2. The peak temperatures at all three points reached the melting point of Ta, indicating that Ta melted at these three locations and produced the IMCs as seen in Fig. 8. Fig. 13c showed the temperature history curves corresponding to joint 3. The peak temperatures of the points at the top and middle of the Ta/FZ interface (6823.5°C and 3712.3°C, respectively) both exceeded the melting point of Ta. The melting depth of joint 3 in Fig. 9 was shallow and Ta in the bottom of the Ta/FZ was solid state due to its lower peak temperature (1581°C < 3020°C). This was agreed quite well with the results of numerical simulation results.

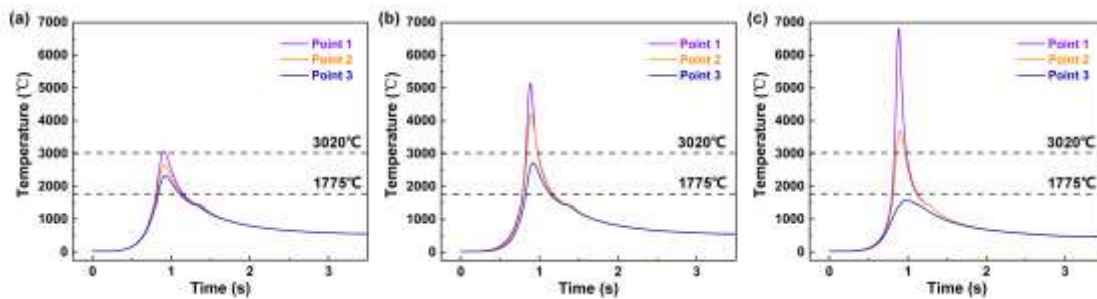


Fig. 13 The temperature history of the selected points marked in Fig. 12: a joint 1; b joint 2; c joint 3.

3.4 Mechanical properties

Fig. 14 showed the microhardness distribution along selection regions for three joints. The average hardness values of 304SS and Ta base metal were 180 HV and 120 HV, respectively. The hardness in the fusion zone and interface was higher than those of base materials due to the formation of $\text{Fe}_2\text{Ta}+\text{Fe-Cr}$ solution. The hardness of joint 2 and joint 3 was larger than that of joint 1 due to the larger amounts of IMCs generated in FZ as seen in Figs. (7-9). Furthermore, the hardness at the Ta/FZ interface was higher than the fusion zone due to the higher volume of generated IMCs transition layer (Fe_2Ta or $\text{Fe}_2\text{Ta}+\text{FeTa}$). In the FZ, the hardness fluctuated within a certain range since the FZ was composed of a Fe-Cr solution matrix and Fe_2Ta brittle phase. The Fe_2Ta brittle phase had a higher hardness than the Fe-Cr solution and this finally led to the inhomogeneous

hardness distribution.

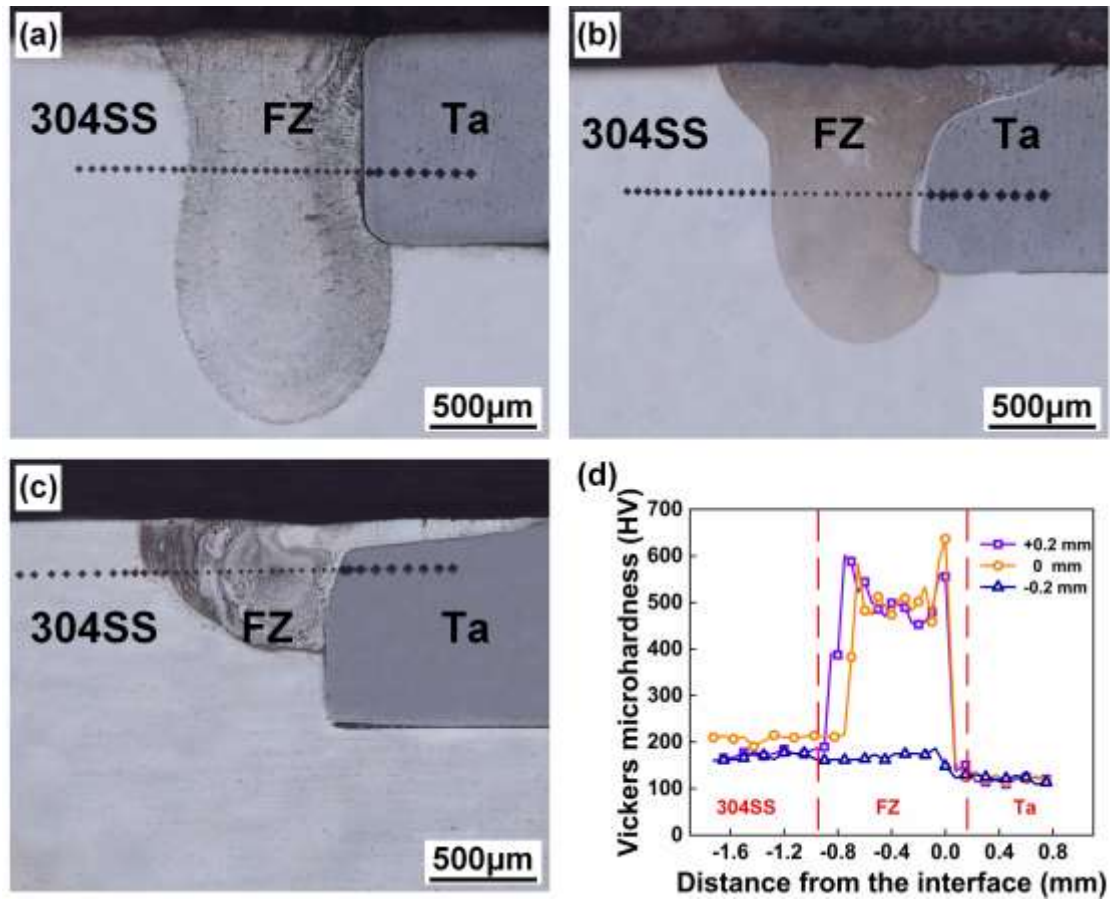


Fig. 14 Microhardness profiles of the joints with different laser beam offsets: (a-c) hardness measurement points of joint 1, joint 2, and joint 3, respectively; d hardness distributions of three joints.

Fig. 15 showed the tensile strength of Ta/304SS joints obtained with different laser beam offsets. The tensile strength increased firstly and then sharply decreased as the laser beam offset further increased. The tensile strength of the joints reached the largest value when laser beam offset was -0.2 mm (308.3 MPa, 59.9% of the value of 304SS and 65.3% of the value of Ta). The maximum strength of the joints had reached the strength level obtained by the electron beam welding [13, 14].

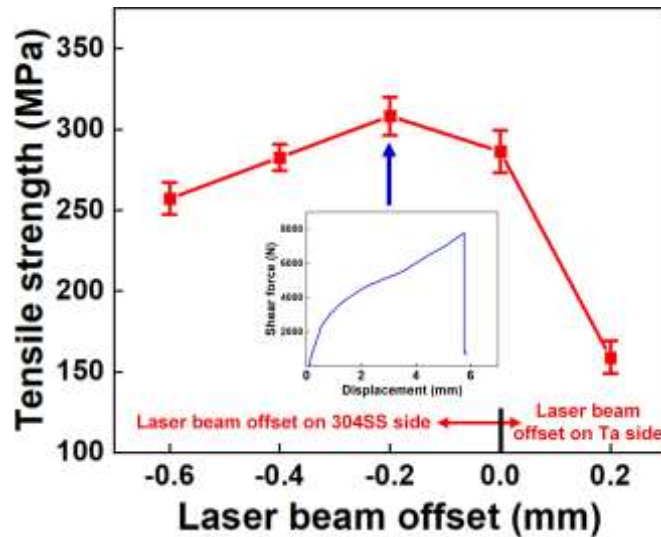


Fig. 15 Tensile strength of the joints produced at different offsets.

Fracture behaviors of these three joints were presented in Fig. 16. Corresponding EDS analyses at selected regions were presented in Table 7. Figs. 16(a-c) depicted the whole fractured surfaces for three joints and it could be found that the 304 stainless steel tube was pulled out from the tantalum cylinder. For further investigating the fractured details of these three joints, the fractured interface in the selected regions was observed and corresponding results were shown in Figs. 16(d-l).

Figs. 16(d-f) showed the fracture paths of these joints. Relevant EDS analyses were performed to confirm the phase components and the results were listed in Table 7. The joint was fractured along with the interface, as the laser beam offset was -0.2 mm and 0 mm. When the laser beam offset became +0.2 mm, the joint was fractured along the FZ+partial FZ. Figs. 16(g-i) showed the fracture interface of these joints. For joint 1, the Fe_2Ta was left at the fractured interface in the FZ side. This indicated that the interface was fractured along the Fe_2Ta layer or $\text{Fe}_2\text{Ta}/\text{Ta}$ interface. For joints 2 and 3, the FeTa was left at the fractured interface in the FZ side and this proved that the interface was fractured along the FeTa layer or FeTa/Ta interface.

To better clarify the fracture behaviors for these joints at the Ta side, the morphology of the

corresponding fracture surfaces was observed and the SEM images were shown in Figs. 16(j-l). Fig. 16j showed the fracture surface of joint 1 and the Fe₂Ta (EDS results showed that Point 4 was composed of 78.88 at.% (Fe + Cr) and 21.12 at.% Ta) was detected at the surface. It indicated the fracture occurred in the Fe₂Ta layer, combined with the Fe₂Ta was observed at the FZ side of fractured interface as shown in Fig. 16g. Fig. 16k revealed the fractured surface for joint 2. The fracture occurred in the FeTa layer since the fracture surface of the Ta side had a composition of 47.45 at. % (Fe + Cr) and 52.55 at. % Ta as shown in Table 7, while the FeTa was also found at the FZ side of the fracture interface as shown in Fig.16 h. Fig. 16l demonstrated the fractured surface of joint 3 at the Ta side. FeTa was detected in the surface since point 6 was composed of 38.96 at. % (Fe + Cr) and 61.04 at. % Ta. Moreover, the FeTa was also observed at the FZ side of the fracture interface as shown in Fig. 16i, this demonstrated that fractured occurred in the FeTa layer. These results implied that the interface joined with the single Fe₂Ta layer had higher strength than that of Fe₂Ta + FeTa.

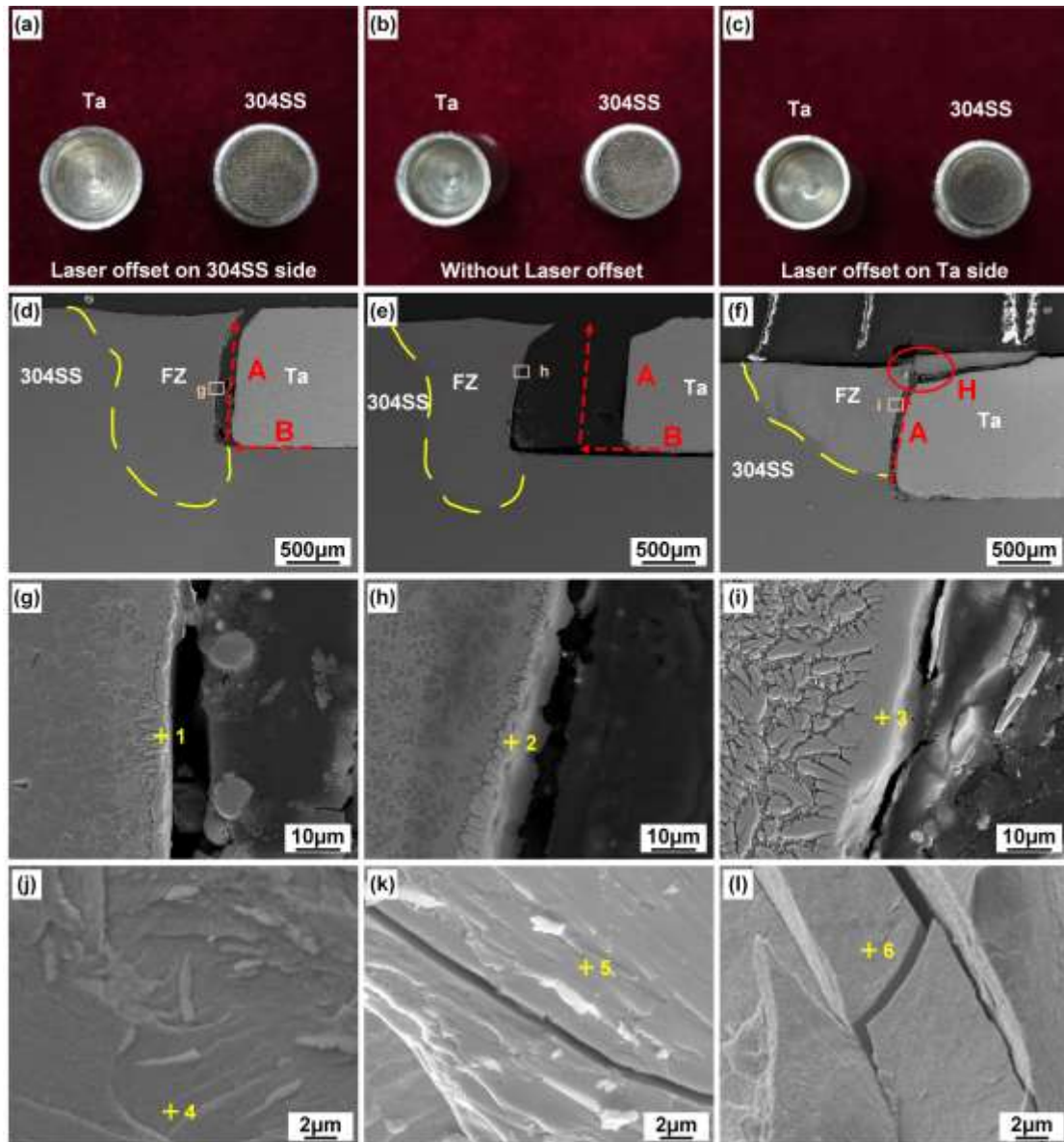


Fig. 16 Fracture behaviors for the joints obtained with different laser beam offsets: (a-c) macro fractured surfaces for three joints; (d-f) fractured paths and locations for three joints; (g-l) fractured surfaces at Ta side for three joints.

Table 7 Component of different points in Fig. 16 (at.%).

Position	Fe	Ta	Cr	Possible phases
1	59.67	28.57	11.76	Fe ₂ Ta
2	36.99	51.33	11.68	FeTa
3	46.26	50.37	3.37	FeTa
4	64.38	21.12	14.50	Fe ₂ Ta
5	35.61	52.55	11.84	FeTa
6	32.07	61.04	6.89	FeTa

4. Conclusions

Tantalum cylinder and 304 stainless steel tube were successfully joined by laser welding under various laser beam offsets (-0.2 mm, 0.2 mm laser beam offset on 304SS side; 0 mm, center; +0.2 mm, 0.2 mm laser beam offset on Ta side). The weld formations, microstructure, and mechanical properties were investigated and the following conclusions were obtained:

(1) Satisfactory appearances of the joints were obtained. When the laser beam offset from 304SS to Ta, the penetration depth of FZ became shallower and partial melting of Ta base materials occurred when the laser was center and 0.2 mm laser beam offset on Ta side.

(2) Fe-Cr solid solution and brittle IMC Fe_2Ta formed in the FZ. The content of Fe_2Ta in the FZ and interfacial IMC thickness were increased as the laser beam offset on Ta side. IMC of Fe_2Ta would be also generated in the Ta/FZ interface in the joints produced under the laser beam offset of -0.2 mm. When the laser beam offsets were 0 and +0.2 mm, FeTa would be newly produced adjacent to Ta base materials.

(3) Numerical simulation results showed that the interfacial peak temperatures increased when the laser beam offset from 304SS to Ta. In addition, duration at high temperature was improved. With these two combined reasons, more Ta base material was melted and thicker IMC was generated.

(4) Fractured behaviors showed that two different fractured paths appeared, namely that interface and interface + partial FZ. The highest joint strength of 308.3 MPa was obtained when the laser beam offset was -0.2 mm under the fractured paths of the interface. This indicated that single Fe_2Ta with smaller thickness was more beneficial for the improvement of joint strength.

Availability of data and material The author confirm that the data and material supporting the findings of this work are available within the article.

Code availability Not applicable.

Authors' contributions All authors contributed to the study conception and design. Material preparation, data collection and analysis were performed by Xiangyi Meng, Fan Song. The first draft of the manuscript was written by Xiangyi Meng and Hongbo Xia. Investigation was performed by Xi Chen and Xiaoye Zhao. Writing-reviewing and editing was finished by Bo Chen, Xiaoguo Song, and Caiwang Tan. All authors read and approved the final manuscript.

Ethics approval Appropriate.

Consent participate All authors approved the manuscript to participate.

Consent for publication All authors approved the manuscript to publication.

Funding The authors would like to acknowledge the financial support National Natural Science Foundation of China (Grant No. 52105405, No. 52005132), Jiangxi Key Laboratory of Forming and Joining Technology for Aerospace Components (No. EL202180263), China Postdoctoral Science Foundation (No. 2021M702423), Natural Science Foundation for Excellent Young Scholars of Shangdong Province (No. ZR2021YQ30).

Declarations

Conflict of interest The authors declare no competing interests.

Reference

- [1] Wei, Chen, Zhang, Ding, Li, Yao, (2018) Plasma surface tantalum alloying on titanium and its corrosion behavior in sulfuric acid and hydrochloric acid. *APPLIED SURFACE SCIENCE* 441:448-457.
- [2] Ng, Mok, Man, (2015) Effect of Ta interlayer on laser welding of NiTi to AISI 316L stainless steel. *Journal of Materials Processing Tech* 226:69-77.
- [3] Sallamand, P., Daloz, D., Vignal, V., Grevey, Bendaoud, I., Erasmus-Vignal, (2015) Microstructural and micro-electrochemical study of a tantalum-titanium weld interface. *Materials & Design* 974-985.

- [4] Niu, Chen, Wang, Yang, Guo, Zhu, Wang, (2017) Preparation and thermal shock performance of thick α -Ta coatings by direct current magnetron sputtering (DCMS). *Surface and Coatings Technology* 321:19-25.
- [5] Masumoto, Asada, Hasuyama, Nishio, Kato, Mukae, (1997) Diffusion bonding of tantalum and stainless steel. *Welding International* 11:110-120.
- [6] Qiao, Fang, Wu, (2022) Effect of pulsed power ultrasonic vibration on keyholing/penetrating capability in waveform-controlled plasma arc welding. *Welding in the World* 66:529-539.
- [7] Sisodia, Gáspár, Draskóczi, (2020) Effect of post-weld heat treatment on microstructure and mechanical properties of DP800 and DP1200 high-strength steel butt-welded joints using diode laser beam welding. *Welding in the World* 64:671-681.
- [8] Chen, Shen, Gao, Zeng, (2020) Influence of welding angle on the weld morphology and porosity in laser-arc hybrid welding of AA2219 aluminum alloy. *Welding in the World* 64:37-45.
- [9] Zhang, Wang, Zhang, Guo, Na, (2019) The mechanical properties and interface bonding mechanism of Molybdenum/SUS304L by laser beam welding with nickel interlayer. *Materials & design* 108002.
- [10] Hajitabar, Naffakh-Moosavy, (2017) Electron beam welding of difficult-to-weld austenitic stainless steel/Nb-based alloy dissimilar joints without interlayer. *Vacuum* 146:170-178.
- [11] Bin, Ting, Yuzhao, Siyuan, Jian, Jicai, (2021) Interfacial strengthening mechanism of electron beam welding-brazed TZM/30CrMnSiA joint with a vanadium interlayer. *Materials Science and Engineering: A* 141369.
- [12] Gao, Li, Liu, Wang, Yu, (2020) Effect of laser offset on microstructure and mechanical properties of laser welding of pure molybdenum to stainless steel. *International Journal of Refractory Metals and Hard Materials* 88:105186.
- [13] Sang, Li, Wang, Ding, Tang, Xiong, (2019) Microstructure and mechanical properties of electron beam welded joints of tantalum and GH3128. *Materials Science & Engineering A* 768:138431.
- [14] Chen, Zhang, Yuan, Deng, (2013) Microstructure and Properties of Electron Beam Welded Tantalum-to-Stainless Steel Joints. *Rare Metal Materials and Engineering* 42:914–918.
- [15] By, Hz, Lw, Ct, Hx, Bo, Xs, (2020) Interfacial microstructure and mechanical properties of laser-welded 6061Al/AISI304 dissimilar lap joints via beam oscillation. *Journal of Materials Research and Technology* 9:14630-14644.
- [16] Shabalín, Igor, (2014) *Ultra-High Temperature Materials I*, Springer Netherlands
- [17] Ninpetch, Kowitwarangkul, (2019) A numerical study on the thermal transient model with moving laser heat source of AISI 304 stainless steel plate. *Materials Today: Proceedings* 17:1761-1767.
- [18] Xia, Tan, Tian, Meng, Ma, (2020) Influence of shielding gas on microstructure and mechanical properties of laser welded–brazed Al/steel lapped joint. *Journal of Manufacturing Processes* 54:347-358.